Topological defects in polycrystalline hexosomes from β-cyclodextrin fatty esters

Jean-Luc Putaux, Christine Lancelon-Pin, Luc Choisnard, Annabelle Gèze,
Denis Wouessidjewe

Topological defects in polycrystalline hexosomes from β-cyclodextrin fatty esters

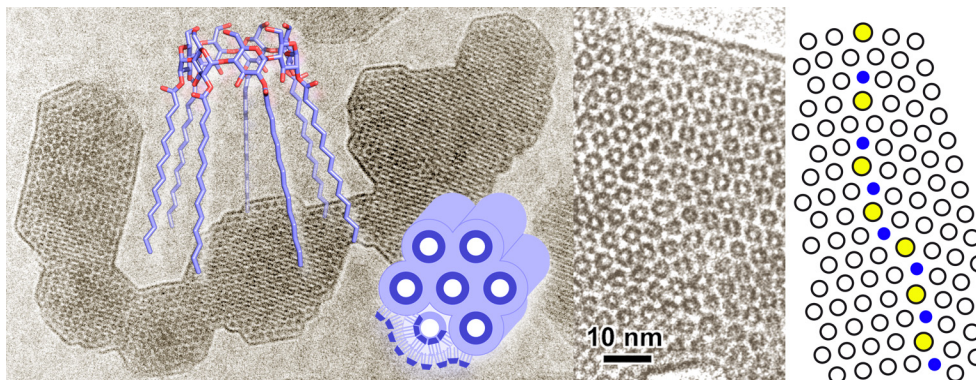Jean-Luc Putaux[a],*, Christine Lancelon-Pin[a], Luc Choisnard[b], Annabelle Gèze[b], Denis Wouessidjewe[b]

a Univ. Grenoble Alpes, CNRS, CERMAV, F-38000 Grenoble, France
b Univ. Grenoble Alpes, CNRS, DPM, F-38000 Grenoble, France

* Corresponding author: jean-luc.putaux@cermav.cnrs.fr

Abstract

Colloidal nanoparticles were prepared by aqueous self-assembly of amphiphilic β-cyclodextrins (βCDs) acylated on their secondary face with C_{14} chains to a total degree of substitution of 7.0, via a thermolysin-catalyzed transesterification process. The small-angle X-ray scattering pattern of the nanoparticles was consistent with a reverse hexagonal organization. Cryo-transmission electron microscopy images revealed particles with spectacular tortuous shapes and consisting of misoriented domains with a regular columnar hexagonal structure, separated by sharp interfaces. Edge dislocations as well as a variety of stepped tilt grain boundaries (GBs) composed of symmetrical and asymmetrical sections, together with one twist GB, were identified from axial views of the columnar organization. The tilt GB structure was analyzed using the concepts of coincidence site lattice and structural units developed to describe the atomic structure of interfaces in various types of polycrystals. The tilt GBs were described using sequences of βCD–C_{14} columns that differed by the number of neighboring columns (5, 6 or 7) and exhibiting distinctive contrasts. To our knowledge, this is the first time that these types of topological defects are described at the nanometric scale by direct observation of colloidal polycrystalline hexosomes of self-organized amphiphiles.

1 Introduction

One major challenge of nanomedicine is the elaboration of "nanovehicles" that deliver active compounds to a targeted site, at a sufficient concentration and without early degradation, in order to maximize the efficiency of the substance while limiting secondary effects. In the recent years, among a wide variety of colloidal vectors of bioactive molecules, liquid crystalline nanoparticles such as the so-called cubosomes or hexosomes[1-5] have attracted a significant attention due to their versatility as delivery systems of antifungal infection agents,[6] contrasting agents for theranostic applications[7-10] or in food additives,[11] to name but a few examples. For a better understanding of the encapsulating capacity and in order to optimize their formulation and lyoavailability, the knowledge of the morphology and molecular organization of these particles is crucial. Cryo-transmission electron microscopy (cryo-TEM) has been the technique of choice to directly visualize the shape, size distribution and ultrastructure of the colloidal nanosystems,[1,12-14] in conjunction with dynamic light scattering (DLS) and small-angle X-ray scattering (SAXS) analyses.

Cyclodextrins (CDs), obtained by enzymatic conversion of starch by the CD glycosyl transferase, are macrocyclic oligosaccharides composed of $\alpha(1\rightarrow4)$-linked glucosyl units. The so-called α-, β- and γCDs, composed of 6, 7 and 8 glucosyl units, respectively, have been considered as building blocks in a variety of nanodevices used for drug delivery.[15-17] Since hydrophobic molecules can be entrapped in the apolar cavity of the CD, a higher solubility, stability or absorption of a large variety of drugs can be achieved.[18] Some inclusion compound products are commercial, which attests to the biocompatibility and safety of the CDs and their hydrophilic derivatives.

CDs can be chemically modified to prepare amphiphilic derivatives that have attracted a significant interest.[17,19-21] They are prepared by grafting hydrophobic substituents on the primary and / or secondary hydroxy groups of the glucosyl units and can be designed to be incorporated in model bilayer membranes,[22-24] or to form aggregates that encapsulate and carry bioactive drugs to specific targets.[25-26] For instance, amphiphilic CDs have been prepared by grafting alkyl chains with different lengths on the secondary hydroxy groups of the CD, either chemically[19,27,28] or using thermolysin to catalyze the transesterification of vinyl fatty ester donors.[29,30] Upon nanoprecipitation, depending in the formulation and process parameters, these derivatives self-organize into nanoreservoirs or solid nanoparticles[31-34] whose drug encapsulation and release properties were evaluated *in vitro* and *in vivo* as potential long-circulating nanocarriers for vascular administration.[33-38]

In previous reports, we have described the morphology and structure of nanoparticles prepared by self-organization of a series of $\beta CD–C_n$ (n = 8, 10, 12, 14) amphiphilic derivatives with various total degrees of substitution (TDS), after dissolution in acetone and nanoprecipitation in water.[30,32,39] The particles were characterized by cryo-TEM imaging of quench-frozen aqueous suspensions and

SAXS. Two types of morphologies and ultrastructures were observed depending on the TDS of the parent derivative. The molecules with TDS < 5 formed nanospheres with an onion-like multilamellar organization whereas those with TDS > 5 self-assembled into barrel-like (n = 8, 10, 12) or more tortuous (n = 14) particles with a columnar inverse hexagonal structure. Ultrastructural models of both structures were proposed based on the analysis of the contrast distribution in cryo-TEM images showing different projections of the lattices.[40]

Remarkably, the nanosystems formed from βCD–C$_{14}$ with TDS = 7.0 exhibited unusual facetted shapes and were composed of several domains (or "grains") with different orientations with respect to one another, separated by sharp interfaces.[40] The present report focuses on the description of the morphology and structure of these βCD–C$_{14}$ particles analyzed from high-resolution cryo-TEM images. In particular, we have described the columnar organization in a number of topological defects, namely dislocations and grain boundaries, at the nanoscale, using geometrical concepts (coincidence site lattices and structural units) previously developed to describe the structure of defects and interfaces in various types of polycrystals.

2 Experimental

2.1 Materials

βCDs (Kleptose$^®$) were provided by Roquette Frères (Lestrem, France). Thermolysin (EC 3.4.24.27), a type X protease isolated from *Bacillus thermoproteolyticus rokko*, anhydrous DMSO (99%), and vinyl myristate (95%) were purchased from Sigma-Aldrich (l'Isle d'Abeau Chesnes, France). Acetone (Acros Organics, analytical grade) was from Fischer Scientific (Illkirch, France). The nanoparticles were prepared in ultrapure water (Elga Purelab).

2.2 Synthesis and characterization of the βCD–C$_{14}$ derivative

The βCD fatty ester was biosynthesized according to the procedure previously described by Choisnard et al. that involved C$_{14}$ vinyl esters as acyl donors and thermolysin as biocatalyst.[30-32] The alkyl chains were grafted on the secondary face of the βCD, mostly at the C2 position of the glucosyl units.[29] The βCD fatty ester was analyzed by matrix-assisted laser desorption/ionization mass spectroscopy (MALDI-MS). According to the analytical method described by Choisnard *et al.*,[39] the derivative was characterized by its average molar weight $\overline{M}_n$ and its TDS, as defined by Challa *et al.*[41] The TDS was calculated using the formula given by Choisnard *et al.*[39] The βCD-C$_{14}$ derivative used in the present study was characterized by $\overline{M}_n$ = 2599.5 g mol^{-1} and TDS = 7.0.[40]

2.3 Nanoparticle preparation

βCD–C$_{14}$ nanoparticles were prepared using the solvent displacement method.[42] Ten milligrams of βCD–C$_{14}$ derivative was dissolved in 10 mL acetone to reach a concentration of 1 mg mL^{-1}. The solutions were kept at 25 °C in a double envelope set-up and poured into an equal volume of distilled water under magnetic stirring (500 rpm). The nanoparticles spontaneously formed and the organic solvent was evaporated under reduced pressure. The aqueous suspension was concentrated to 1.5 mg mL^{-1} at 40 °C under vacuum, filtered through 0.8 μm filters and kept at room temperature. The sample was further concentrated by centrifugation (9600 g) to about 5-10 mg mL^{-1} for cryo-TEM observation and SAXS analyses. The samples were prepared in triplicates.

2.4 Cryo-transmission electron microscopy (cryo-TEM)

Cryo-TEM specimens were prepared by quench-freezing thin liquid films of a 5-10 mg mL^{-1} nanoparticle suspension formed on Pelco NetMesh lacy carbon films into liquefied ethane, using a Leica EM-GP workstation. Once mounted in a Gatan 626 cryoholder precooled with liquid nitrogen, the specimens were observed at low temperature (-180 °C), under low dose illumination, using a Philips CM200 'Cryo' microscope operating at 80 kV. The images were recorded on Kodak SO163 films.

2.5 Small-angle X-ray scattering (SAXS)

SAXS analyses were performed on the BM02 beamline at the European Synchrotron Radiation Facility (Grenoble, France). The concentrated suspension was poured into a glass tube (3.0 mm outer diameter). The scattering pattern was recorded at room temperature, during 50 s, at an energy of 16.62 keV ($\lambda = 0.0764$ nm) with a CCD detector placed at a distance of 24 cm, and calibrated using a silver behenate standard. The SAXS profile was calculated as a radial average of the two-dimensional pattern and the profile of a glass tube containing only water was subtracted. The diffraction peaks were fitted with Gaussian functions and the unit cell parameters were calculated using a least-squares regression.
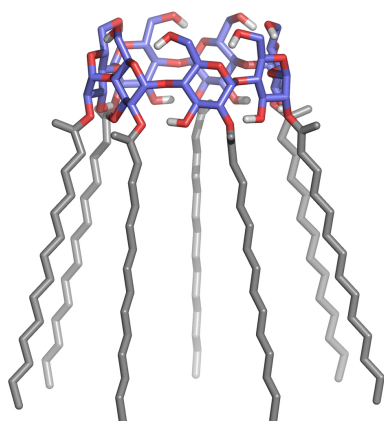
Scheme 1. Idealized structure of one molecule of βCD–C$_{14}$ with TDS = 7. The alkyl chains, drawn in gray, are grafted at the C2 position on the secondary face of the βCD.[29] Hydrogen atoms were omitted for clarity.

3. Results

3.1. Morphology and ultrastructure of the βCD–C₁₄ particles

The synthesis of the βCD–C₁₄ derivative with TDS = 7.0 was described in the Experimental Section and a schematized 3D model of the molecule is shown in **Scheme 1**. The particles prepared by nanoprecipitation, briefly presented in our previous article,[40] exhibit a variety of shapes. In particular, a significant number of particles have a peculiar tortuous and facetted morphology (**Fig. 1a**). At higher magnification, lattice lines are visible whose patterns depend on the shape and orientation of the particles with respect to the electron beam. Most interestingly, a given tortuous particle can exhibit different patterns, suggesting that it consists of distinct domains with different mutual orientations. This is illustrated, for example, by the particle showed in **Fig. 1c,** as well as those in Supplementary Information **Fig. S1**. Some regions of the particles exhibit sets of parallel fringes whereas others contain highly contrasted hexagonal patterns (**Fig. 1b** and **1d**), the neighboring grains being separated by more or less clearly defined interfaces.
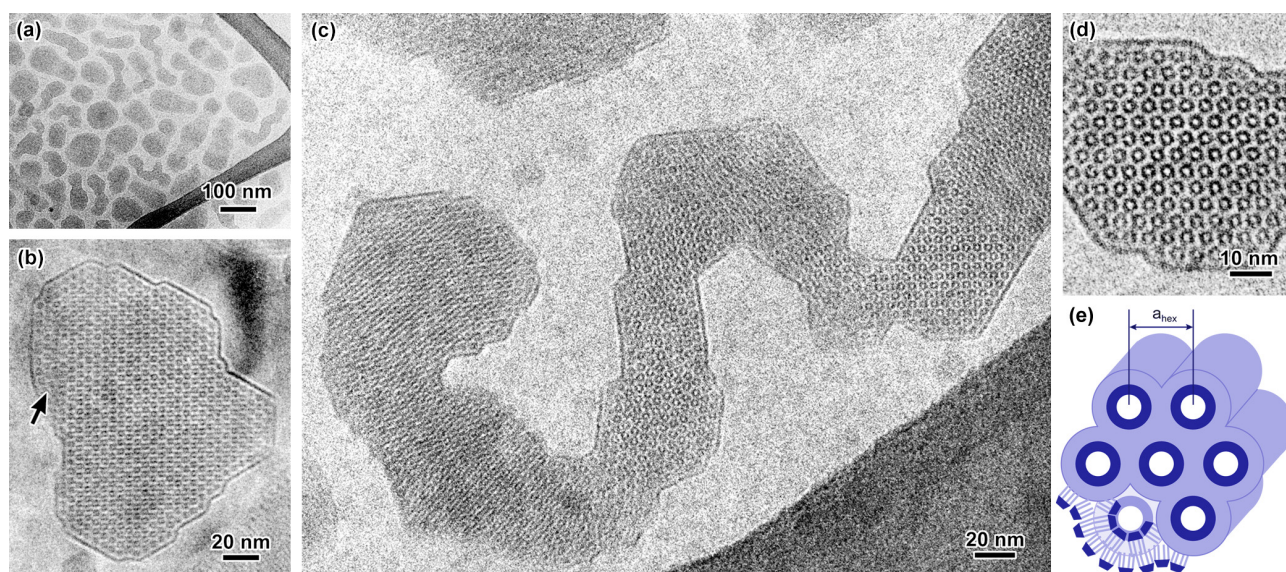

Figure 1. Cryo-TEM images of particles prepared by nanoprecipitation of the βCD–C₁₄ derivative with TDS = 7: a) general view: note the presence of elongated and tortuous particles; b,c) examples of facetted particles showing the hexagonal organization of βCD–C₁₄ columns. In b, the particle is made of only one grain and the hollow columns appear as dark circles seen in axial view. The arrow points to one structural defect near the edge of the particle. In c, the particle is composed of several domains misoriented with respect to one another, separated by grain boundaries. Various projections can be observed depending on the orientation of the grains. d) Higher magnification image of the hexagonal network of βCD–C₁₄ columns seen along the column axis. e) Scheme describing the organization of βCD–C₁₄ molecules in the projection of the columns and in the outer layer in contact with water revealed by the continuous dark fringe in image d. a_{hex} is the parameter of the two-dimensional hexagonal unit cell.

Figure 2. SAXS profile recorded from a suspension of βCD–C$_{14}$ particles that confirms the hexagonal organization. The q_i/q_1 ratios are indicated above each peak, with $q_1 = 1.49$ nm^{-1}.
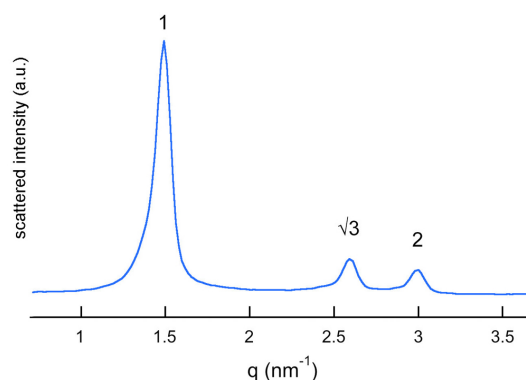
In addition, as seen in **Fig. 2**, the SAXS profile recorded from a suspension of βCD–C$_{14}$ particles contains three main peaks with a series of q_i/q_1 ratios (1, $\sqrt{3}$, 2) characteristic of a columnar reverse hexagonal structure.[40,43] From this profile, we calculated the hexagonal unit cell parameter $a_{hex\text{-}SAXS} = 4.90$ nm. By analogy with the so-called H$_{II}$ phase proposed to describe the self-assemblies of various amphiphiles,[44-47] the βCD–C$_{14}$ molecules are likely organized into columns with the alkyl substituents radiating outward and a central cavity hosting water molecules (**Fig. 1e**). Assuming that the hexagonal pattern of dark rings visible in some grains corresponds to an axial projection of the columns, the hexagonal lattice parameter is the distance between the centers of two neighboring columns. From the cryo-TEM images, we measured the parameter $a_{hex\text{-}TEM} = 4.8$ nm (**Fig. 1d**), in good agreement with the value measured by SAXS.

The origin of the contrast in the cryo-TEM images of βCD–C$_n$ nanoparticles has been explained in detail in our previous article, in particular for edge-on projections of the hexagonal columnar organization.[40] Here, our description of the structure focuses on the images showing end-on projections, *i.e.* when the electron beam is parallel to the column axis (**Fig. 1e**). Briefly, at an acceleration voltage of 80 kV and with a defocus of the objective lens ranging between -2.0 and -3.0 μm, the regions with the highest density and a repeat distance of around 4-5 nm in the lattice images are transferred with a dark contrast.[40] Assuming that the model proposed in **Fig. 1e** is correct and considering that the βCD macrocycle and ester bonds contain oxygen atoms (**Scheme 1**), the electron density of the cylinders formed by the superimposition of βCD moieties should be higher than that of the corona containing only alkyl chains. Therefore, the central part of the column, supposedly containing water molecules, should be clear, while the surrounding dark ring would correspond to the superimposition of βCD macrocycles, each ring separated by a continuous phase of alkyl chains with an intermediate gray level. The cryo-TEM images also reveal a dark outline that surrounds all the particles regardless of their size and shape (**Fig. 1** and **Fig. S1**). Consistent with a mechanism previously described for the stabilization of various micellar structures,[44,45,48] a continuous layer of βCD–C$_{14}$ should cover the particle surface, with the hydrophilic primary face of the βCD moiety oriented outward, in contact with water, thus ensuring a good colloidal stability (**Fig. 1e**).[40]

TEM images of dry preparations of the βCD–C$_{14}$ particles observed at low temperature are shown in **Fig. S2**. Since the images were recorded at a lower magnification to limit the radiation damage, the resolution is not as good as that in the cryo-TEM images. However, the presence of various sets of lattice fringes attests to the partial stability of the ultrastructure upon drying. In some regions, the particle orientation is such that an axial projection of the hexagonal lattice can be recognized (**Fig. S1a**).

3.2 Description of the topological defects

Two types of topological defects will be described in the following that could directly be visualized in cryo-TEM images of axial projections of the columnar domains: edge dislocations (**Section 3.2.1**) and tilt grain boundaries (**Section 3.2.2**). Many other types of linear and two-dimensional defects likely exist but they could not be analyzed due to their misorientation with respect to the observation direction, with the exception of one twist grain boundary (**Section 3.2.3**). The organization of βCD–C$_{14}$ columns is such that, in axial projection, the two-dimensional hexagonal lattice can be described by means of (x,y) coordinates along the two [10] axes of the unit cell defined by parameter $a_{hex} = b_{hex}$ and angle $\gamma = 120°$.

3.2.1 Edge dislocations

Two examples of dislocations are shown in **Fig. 3a** and **3d.** The complete particles from which these images were extracted are shown in **Fig. S1d** and **S1e**. The dislocations were indirectly detected by the small bending of the lattice induced by the displacement field around their core and the nature of the dislocations was determined by drawing Burgers circuits.[49] Two possible but equivalent circuits were drawn (**Fig. 3c** and **3f**) from which a similar **b**$_{(1,0)}$ Burgers vector was deduced, that correspond to the distance between two columns along a (10) plane, equal to a_{hex}. Since the contrast of the columns did not seem to be significantly modified around the defect, we assumed that the dislocations were of pure edge nature, *i.e.* their Burgers vectors were normal to the dislocation lines, without any additional twist component along the column direction.

Since the contrast in the core itself was not clearly defined, we marked the position of each visible column with their 6 neighboring columns in the hexagonal lattice. The core region was then described by a coordination defect that would be composed of the association of two different columns, one with 5 neighbors and the other with 7. Although putative in the present case, the geometry of this defect is likely since it is similar to those described for edge dislocations in materials with two-dimensional hexagonal lattices, such as block copolymer films,[50-52] charged polymer colloids,[53] butterfly eyes,[54-55] magnetic bubble arrays[56] or graphene layers.[57]

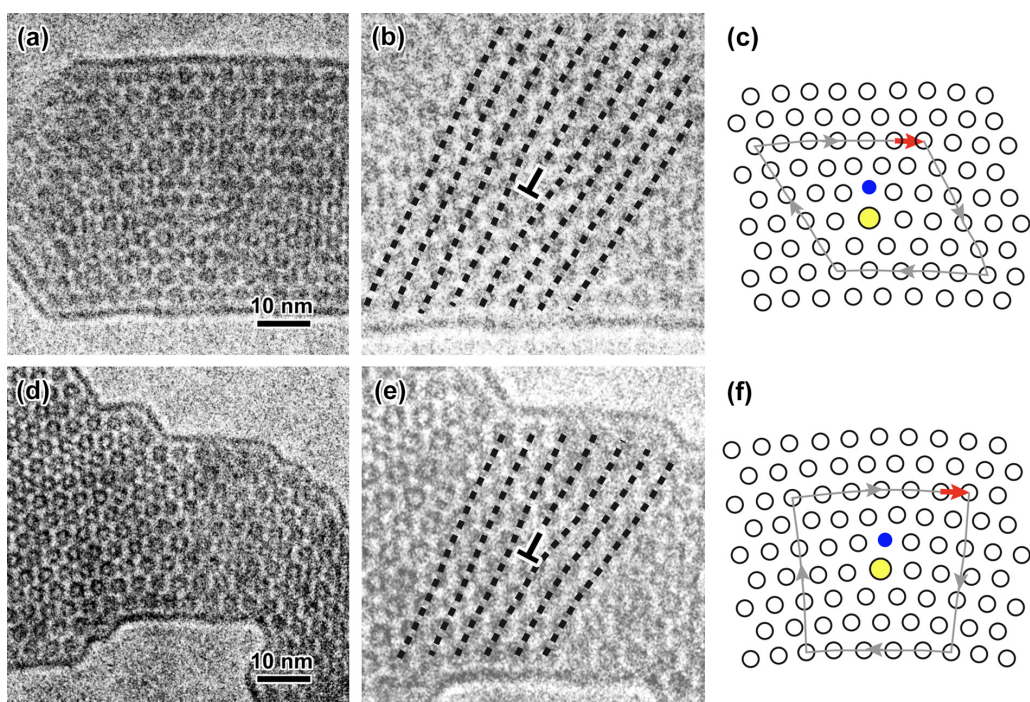**Figure 3.** Examples of $b_{(1,0)}$ edge dislocations in βCD–C$_{14}$ hexosomes: a,d) cryo-TEM images; b,e) enlargement of images a and b onto which the traces of (10) planes have been superimposed. The location of the edge dislocation is indicated with a ⊥ symbol in front of the extra half-plane. c,f) Corresponding models of column organization. The black circles are projections of βCD–C$_{14}$ hollow columns organized in a hexagonal structure. The blue and yellow disks are columns with 5 and 7 neighboring columns, respectively. Two possible Burgers circuits are drawn around the dislocation cores, both resulting in the same $b_{(1,0)}$ Burgers vector (red arrow). Larger views of the particles are given in **Fig. S1d,e**.

3.2.2 Tilt grain boundaries

A so-called tilt GB separates two grains misoriented around a rotation axis that is parallel to the boundary plane.[58] In the present case, the tilt axis is also parallel to the axis of the columns formed by the βCD–C$_{14}$ molecules. Since the hexagonal unit cell contains three sets of (10) planes, the rotation angle between two adjacent grains can be defined using several conventions. In the present article, the tilt angle θ was defined as the smallest angle between a set of (10) planes chosen in each grain (**Fig. S3**).

The concept of coincidence site lattice (CSL) was developed to describe the structure of simple GBs in a variety of crystalline materials.[59-61] This description can also be applied to the present two-dimensional hexagonal arrangement of βCD-C$_{14}$ columns. A dichromatic pattern is defined as the two interpenetrating crystal lattices, one being rotated by an angle θ with respect to the other around one site common to both lattices. For specific rotation angles, all sites in coincidence form a superlattice, the so-called CSL.[59,62] Examples of such dichromatic patterns and corresponding CSLs for a hexagonal unit cell are shown in **Fig. S4**. The unit cells in each grain are similar lozenges with a 120° angle and, due to the symmetry of the dichromatic pattern, the CSL unit cell is also a hexagonal unit cell described by a homothetic lozenge. The coincidence index Σ is defined by the ratio of the

surface of the unit cell of the CSL to that of one elementary lattice. The CSL planes with lower indices thus contain the highest number of coincidence sites and can be used to define the position of possible low-energy symmetrical tilt GBs.[59]

Examples of symmetrical tilt GBs between domains with a columnar hexagonal structure are shown in **Fig. 4a-d**, using circles and dots that would correspond to columns of self-organized βCD-C_{14} molecules. The GB with the lowest angle, namely $\Sigma = 37$ ($\theta = 9.4°$) can be described using the same 5/7 pair of coordination defects (or structural units – SUs) that was assumed to correspond to the core of the bulk $b_{(1,0)}$ edge dislocations (**Fig. 3c** and **3f**). The $\Sigma = 37$ GB, as well as those corresponding to $\Sigma = 19$ ($\theta = 13.2°$) and $\Sigma = 7$ ($\theta = 21.8°$) can be described by a specific sequence of 5/7 SUs separated by a number of 6-type columns, and their distance decreases with increasing tilt angle. For these three examples, the GB is a mirror plane. For the symmetrical $\Sigma = 13$ ($\theta = 32.2°$) GB, the 5/7 SUs are contiguous and organized in a zig-zag fashion to better minimize the local distortions. In this case, the GB is a mirror + glide plane. These SU sequences are very similar to those proposed to describe the structure of tilt GBs in a variety of two- or three-dimensional polycrystalline materials where atoms, molecules or particles are organized in hexagonal lattices through interactions of very different nature, exemplified in semiconductors,[61] graphene,[63-66] bubble rafts[67] magnetic bubble arrays,[56] block copolymer films,[50,51,68] or the cornea of some butterflies.[54]
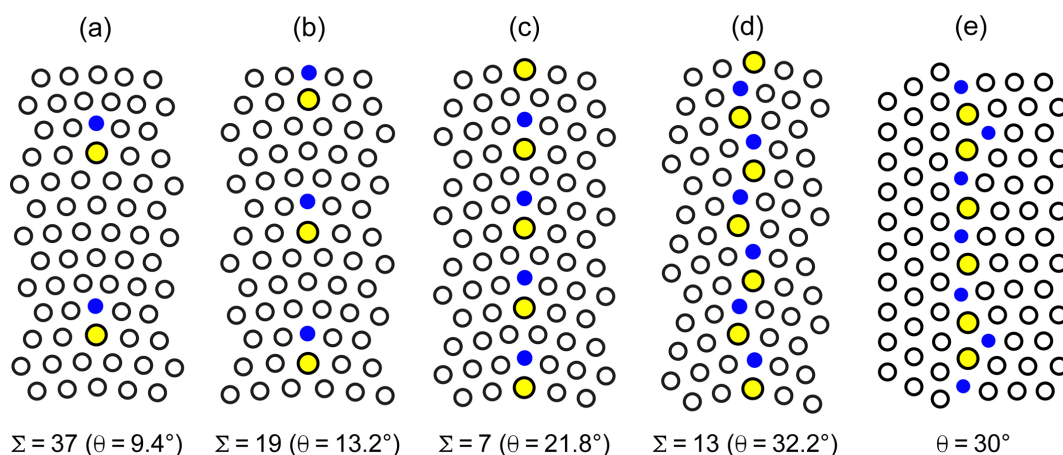

Figure 4. Geometrical models describing tilt GBs, using specific arrangements of SUs. The black circles are axial projections of βCD–C_{14} hollow columns organized in hexagonal lattices. The blue and yellow disks correspond to columns surrounded by 5 and 7 neighboring columns, respectively. The coincidence index Σ and corresponding tilt angle are given. The tilt angle was defined as in **Fig. S2**. For $\Sigma = 37$, 19 and 7, both grains are symmetrical and the GB is a mirror plane. For $\Sigma = 13$, the 5- and 7-type structural units adopt a zig-zag arrangement and the GB is a mirror + glide plane. Strictly, the GB described for $\theta = 30°$ does not correspond to a coincidence. The (10) planes of grain 1 are parallel to the (11) planes of grain 2 but the distances between columns in both types of planes are incommensurable. Only a small portion of the GB is shown in order to introduce new tentative arrangements of SUs.

A special GB model corresponding to a tilt angle $\theta = 30°$ is also shown in **Fig. 4e**. It is asymmetrical and is parallel to one set of (10) plane of grain 1 and one set of (11) planes of grain 2. However, this GB does not correspond to a coincidence. Indeed, the repeat distance of the (11) planes is $2a\cos 30° = a\sqrt{3}$ and is incommensurate with the closest repeat distance along a (10) plane (*i.e.* $2a$). In this type of GB, the mismatch is compensated by specific aperiodic groups of SUs. In the present case, the tentative column arrangement shown in **Fig. 4e**, and referred to as θ_{30}, was inspired by those proposed by Liu and Yakobson[57] and Yazyev[69] for a similar asymmetrical GB in polycrystalline graphene. It also involves 5/7-type SUs organized in two different motifs.

The structure of the various tilt GBs that were observed in the βCD–C_{14} particles was analyzed with respect to these reference structures, using recognizable sequences of 5/7- and 6-type SUs. In various materials, when a GB does not correspond to a perfect coincidence, the deviation from it can be accounted for by so-called secondary GB dislocations.[58] However, we could not use this type of analysis since the GB sections in the hexosomes were rather short, preventing to define a clear reference coincidence over a long distance and draw proper Burgers circuits around defects.

While the images presented in **Figs. 5** and **6** are close-up views of the tilt GBs in selected particles, lower magnification views of the whole corresponding facetted particles are shown in **Fig. S1**. While the contrast of the edge dislocation core was not well defined in the images of **Fig. 3**, the 5 and 7 SUs in GBs were directly recognizable. The core of the 7-type columns appeared to be slightly larger than that of the 6-type columns in the grains (**Fig. 5a, 5d** and **5g**). On the contrary, the 5-type columns appeared as dark dots and not as rings like the 6- and 7-type columns. Considering the more constrained environment, it is likely that the βCD–C_{14} molecules could not organize to form a hollow column as described in **Fig. 1e**. All βCD macrocycles would rather superimpose, forming a single electron-dense column, with the alkyl moieties still pointing outward and facing the neighboring columns.

Four stepped tilts GBs were analyzed in **Fig. 5** and described as composed of portions of reference symmetrical or asymmetrical GBs shown in **Fig. 4**. GB1 in **Fig. 5b** and **5c** is composed of sections of symmetrical $\Sigma = 7$ ($\theta = 23 \pm 1°$) in different planes, while GB2 in **Fig. 5d** and **5e** corresponds to $\Sigma = 13$ ($\theta = 31 \pm 1°$). The GB in **Fig. 5g** and **5h** contains two sections of symmetrical $\Sigma = 7$ in different planes and one portion of $\Sigma = 13$, resulting in a global tilt angle of $23 \pm 1°$. The GB in **Fig. 5j** and **5k** is composed of two sections of θ_{30} separated by a step and one section of symmetrical $\Sigma = 7$ GB, resulting in a global tilt angle of $27 \pm 1°$. Tilted views of this GB highlighting the local distortion of the lattice planes in the vicinity of the boundary are shown in **Fig. S5.** The SU sequence in the stepped GB shown in **Fig. S6** is more complex although short sections from $\Sigma = 7$ and θ_{30} GBs can be recognized ($\theta = 25 \pm 1°$).

A general observation was that the analyzed tilt GBs were not symmetrical and rather exhibited various stepped structures. In addition, the tilt angles were close but not equal to those of the main coincidences defined in **Fig. 4**. However, for the majority of analyzed GBs, Σ typically ranged between 23 and 31°, *i.e.* within the typical angular domain between $\Sigma = 7$ and 13, in line with the CSL model that claims that coincidences with the smallest indices are favored. Lee e*t al.* made a similar observation on the statistics of tilt GBs occurring in the multidomain hexagonal arrays of nanonipples in the eye of the Mourning Cloak butterfly.[62] Energy calculations performed on grain boundaries in GaN semiconductors as a function of tilt angle also showed minima at $\Sigma = 7$ and 13.[61]

The image in **Fig. 6** shows a more complex configuration. A short section of symmetrical $\Sigma = 13$ can be recognized in the continuity of a lower angle section that contains SU sequences corresponding to symmetrical $\Sigma = 19$ and $\Sigma = 31$ ($\theta = 17.9°$) (**Fig. 6c**). Near the region where the GB changes directions, there is an edge dislocation that can still be considered isolated in grain 2 and not part of the GB. Complementary tilted views of this configuration are shown in **Fig. S7**.

3.2.3 Twist grain boundary

A twist GB separates two grains that are misoriented around a rotation axis that is perpendicular to the boundary plane.[58] The image of the particle shown in **Fig. 7** contains a small region where the axial projection of a few $\beta CD–C_{14}$ columns can be recognized, around which the contrast pattern consists of more or less defined concentric fringes. In order to simulate this peculiar pattern, we have superimposed two identical images of a perfect hexagonal pattern of columns. The top image was made semi-transparent and incrementally rotated with respect to the image below. Qualitatively, a satisfactory fit with the experimental image was obtained with a rotation of 8°. This confirmed that the contrast could be explained by assuming that the two grains in the particle were rotated with respected to each other around an axis parallel to the column, thus separated by a twist GB. However, with this projection image, it was not possible to describe the GB itself and, in particular, determine whether it lay perfectly perpendicular to the rotation axis or with a more complex geometry like that of the stepped tilt GBs described in the previous section.
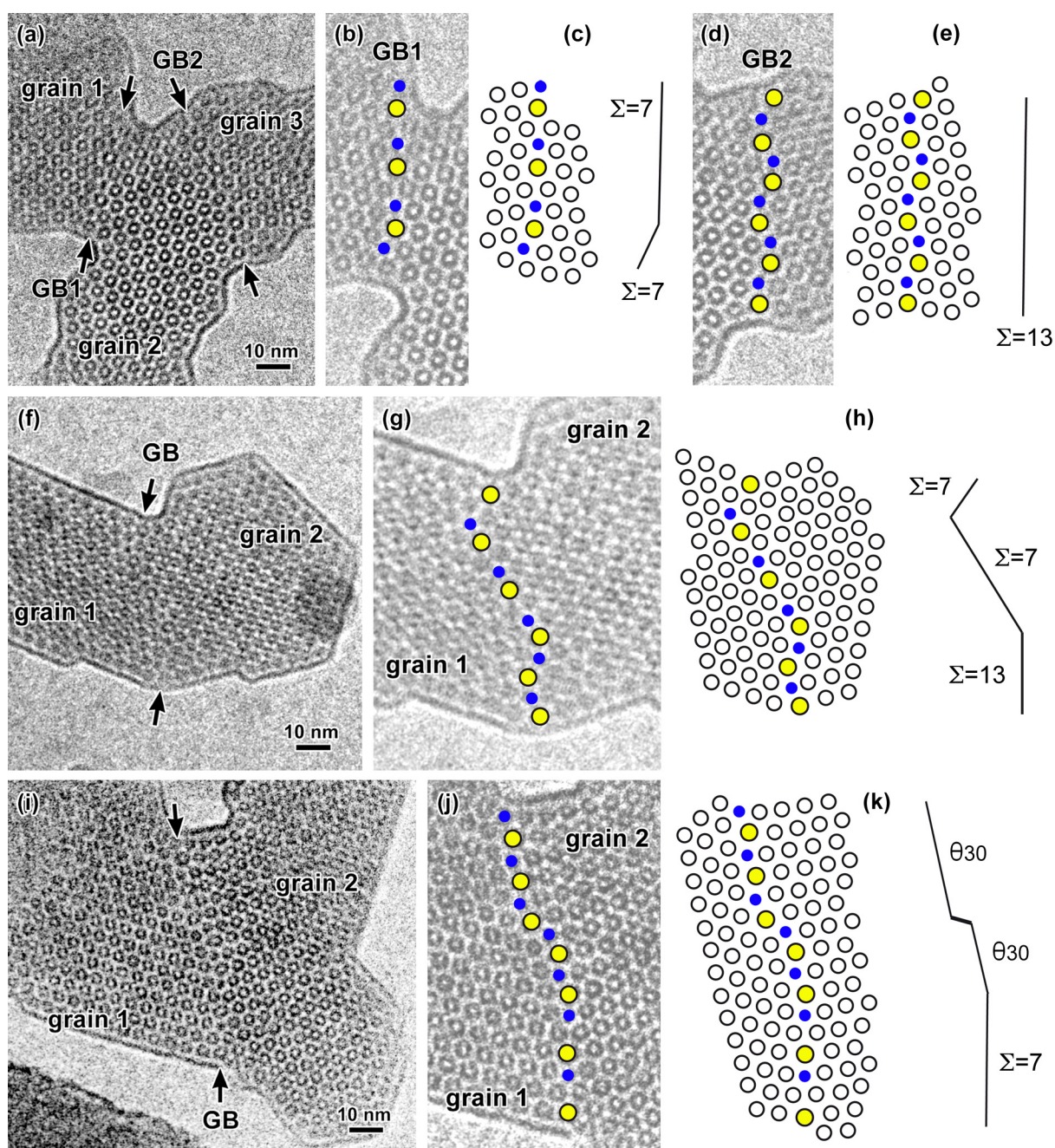
Figure 5. Cryo-TEM images of various stepped tilt grain boundaries (GBs) observed in βCD–C$_{14}$ hexosomes with tentative descriptive models of column organization. The black circles in the schemes are projections of βCD–C$_{14}$ hollow columns organized in a hexagonal lattice. The blue and yellow disks are columns with 5 and 7 neighboring columns, respectively. The tilt angles measured between the adjacent grains are 23 ± 1° (GB1) and 31 ± 1° (GB2) in image a, 23 ± 1° in image f, and 27 ± 1° in image i. In c, e, h and k, local GB planes with corresponding coincidence indices are proposed based on the sequences of SUs defined in the models of perfect GBs (**Fig. 4**). Larger views of the whole particles are available in **Fig. S1a-c**. Additional tilted views of the GB in i are provided in **Fig. S5**.
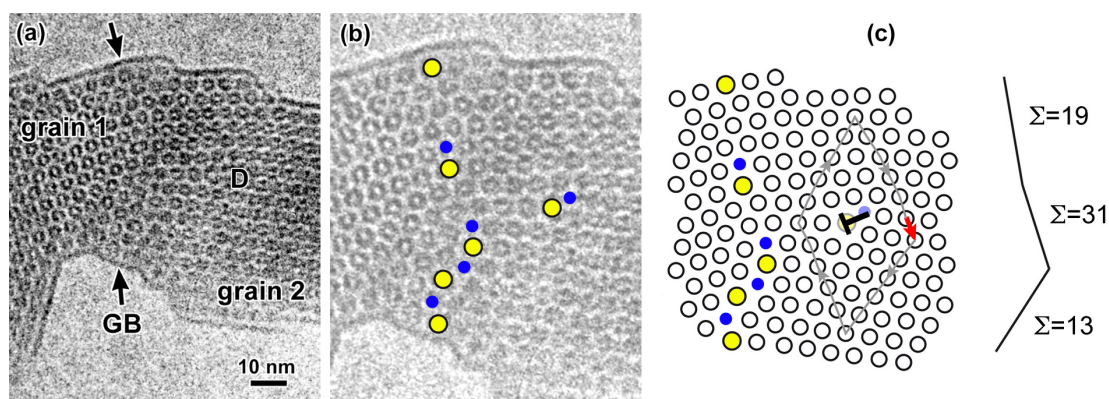
Figure 6. Cryo-TEM images of a stepped tilt grain boundary (GB) and an edge dislocation (D) observed in a βCD–C_{14} hexosome (a,b) with descriptive models of column organization (b,c). The black circles are projections of βCD–C_{14} columns organized in a hexagonal structure. The blue and yellow disks are columns with 5 and 7 neighboring columns, respectively. In c, the Burgers circuit around the dislocation core is drawn in gray and the red arrow indicates the $\mathbf{b}_{(1,0)}$ Burgers vector. The location of the edge dislocation is indicated with a $\perp$ symbol in front of the extra half-plane. A larger view of the particle is shown in **Fig. S1f**. Complementary tilted views are provided in **Fig. S7**.
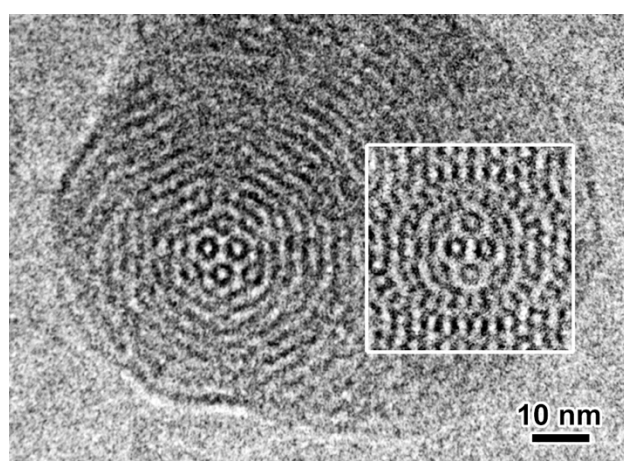

Figure 7. Twist boundary in a βCD–C_{14} hexosome around an axis that is parallel to the βCD–C_{14} column (cryo-TEM image). The projection of the grains rotated with respect to one another is blurred except in the vicinity of the rotation axis. Inset: simulation of the contrast pattern observed in the experimental image: a partially transparent image of a perfect hexagonal network was superimposed on the same image and rotated in plane by 8°.

4 Discussion

To our knowledge, the formation of such complex morphologies has never been reported before for nanoparticles of self-assembled amphiphilic molecules and the question of the mechanism that drives the formation of such convoluted polycrystalline objects stays open. During nanoprecipitation, βCD–C_{14}-rich droplets form upon dilution of the acetonic solution into water. When saturation is exceeded, the molecules self-assemble, forming nuclei that can grow into well-formed mesophases.[70] However, the resulting particles are expected to adopt a shape that would minimize their surface-to-

volume ratio to some extent,[71,72] although there might be a competition with a favorable growth along specific directions of the self-assembled mesophase. This tendency has previously been observed with βCD–C$_8$ and βCD–C$_{10}$ with TDS around 7, that self-assembled into individual barrel-like hexosomes elongated along the column axis.[40] However, a significant number of the βCD–C$_{14}$ particles presented here were multidomain and exhibited shapes for which the surface-to-volume ratio was clearly not minimized. Among the series of tested βCD–C$_n$ derivatives, βCD–C$_{14}$ had the highest hydrophobicity due to the contribution of the longest alkyl moieties and the high degree of substitution (TDS = 7.0) and this characteristic likely promoted a kinematic freezing of the molecular arrangements at room temperature, as soon as a sufficient amount of acetone had been diluted in water upon nanoprecipitation. Indeed, the dislocations and GBs did not spontaneously migrate to the surface of the particles and they were immobilized like in a solid material.

Two mechanisms can be proposed to explain the polycrystallinity of the particles: 1) individual small hexosomes randomly collided in the aqueous suspension and formed stable aggregates; 2) at an early stage of nanoprecipitation, several nuclei simultaneously formed and grew inside βCD–C$_{14}$-rich droplets. The confinement of these small proto-hexosomes in the droplets would promote their clustering into larger particles. The diversity of shape, size and orientation of the constituting domains is in favor of a clustering mechanism. However, the random flocculation of the formed hexosomes in aqueous suspension seems unlikely considering the continuity of the facetted surfaces and the regular layer of βCD–C$_{14}$ molecules covering the particles to preserve the colloidal stability. In addition, the significant number of tilt GBs would require a reorientation of the grains or a reorganization of the columns to yield neighboring grains with a common tilt axis. The early clustering of neighboring proto-hexosomes inside droplets is more likely as long as a residual amount of acetone is available to maintain some molecular mobility. Then, the overall structure is frozen.

To shed additional light on the mechanism at work during particle formation, it would thus be interesting to compare the morphology adopted by the self-assembled βCD-C$_{14}$ molecules when i) the nanoprecipitation is carried at temperatures higher than 25 °C and ii) the particles shown in the present article are submitted to a hydrothermal annealing treatment that may induce structural transition / reordering.[44] If the molecular mobility is increased at a higher temperature, one can expect the topological defects to migrate to the particle surface, and the various domains to coalesce and reorganize into unique hexosomes with a bulkier shape that would minimize their surface-to-volume ratio. Optimizing such annealing treatments may allow for a better control of the particle morphology and ultrastructure for nanomedicine applications.

The columnar inverse hexagonal structure can simply be described as a parallel packing of cylinders. The formation of edge dislocation and tilt boundaries would thus be energetically favorable since all cylinders remain parallel in these configurations. However, we restricted our description to

the topological defects that were conveniently oriented in the ice film, i.e. with the columns aligned parallel to the electron beam direction. Many different grain boundaries existed in many other particles, some of which are visible in the images shown in Supplementary Information, but they were not properly oriented and could not be analyzed. Moreover, in many cases, the GBs could not be analyzed because small twist components likely induced local blurring of the image contrasts. Therefore, since our geometrical description was only successful for a relatively small number of particles of the population, we could not provide any meaningful statistics on the occurrence of such and such type of defects.

Visualizing topological defects in radiation sensitive materials is still a substantial challenge for electron microscopists, which explains why such images are extremely rare in the literature. This study was carried out by recording cryo-TEM images of the nanosystems on photographic films that require a sufficient electron dose in order to achieve a good contrast. There is no doubt that higher resolution information on the particle ultrastructure and the topological defects would be collected using new-generation cryomicroscopes equipped with highly sensitive digital camera and software allowing automated low-dose image recording.[78] Tomographic approaches such as that used to visualize the three-dimensional molecular organization in monoglyceride-based cubosomes[79] would also be helpful to analyze a wider variety of topological defects, making a direct comparison with image simulations from numerical molecular models possible.

5 Conclusions

Recent works have reported on topological defects – namely, disclinations – in facetted liquid crystalline vesicles[73] and striped block polymersomes,[74,75] but little is known about the high-resolution structure of topological defects in soft colloids. Grain boundaries and dislocations have been observed by Hudson and coll. in RuO_4-stained thin films of columnar hexagonal and cubic assemblies of a thermotropic amphiphilic dendrimer.[76,77] More recently, Liu *et al.* have characterized the complex topology of twins and five-fold twin boundaries in double-diamond cubosomes from heteroclusters.[78] However, to our knowledge, this is the first time that topological defects are described in solid hexosome nanoparticles of a self-assembled amphiphile, with a resolution of a few nanometers. Based on cryo-TEM images of projections of the hexagonal structure along the column axis, the organization of βCD–C_{14} assemblies, and the structure of edge dislocations and stepped tilt grain boundaries, were analyzed in particles whose convoluted morphology and polycrystalline structure are likely due to the combination of a clustering taking place in the early stages of nanoprecipitation and a kinematic freezing in a water-rich environment due to the high hydrophobicity of the seven C14 moieties grafted on the secondary face of the βCD macrocycle. The

topological defects in this supposedly "soft" assemblies were surprisingly well described using the concepts of coincidence site lattice and structural units initially defined for solid polycrystalline materials like semiconductors and metals and, due to the hexagonal symmetry of the unit cell, the coordination defects were geometrically similar. All analyzed tilt GBs were described as sequences of 5/7 and 6-type structural units defined with respect to symmetrical boundaries with a high degree of coincidence.

Acknowledgements

References

1   L. Sagalowicz, R. Mezzenga and M. E. Leser, *Curr. Op. Colloid Int. Sci.*, 2006, **11**, 224–229.

2   L. Sagalowicz, S. Acquistapace, H.J. Watzke and M. Michel, *Langmuir*, 2007, **23**, 12003–12009.

3   Y. Chen, P. Ma and S. Gui, *BioMed Res. Int.*, 2014, **2014**, 815981.

4   A. Otte, B.-K. Soh, G. Yoon and K. Park, *Int. J. Pharm.*, 2018, **539**, 175–183.

5   H. M. G. Barriga, M. N. Holme and M. M. Stevens, *Angew. Chem. Int. Ed.*, 2019, **58**, 2958–2978.

6   M. M. Ebersold, M. Petrović , W.-K. Fong, D. Bonvin, H. Hofmann and I. Milošević, *Nanomaterials*, 2018, **8**, 91.

7   X. Mulet, B. J. Boyd and C. J. Drummond, *J. Colloid Interface Sci.*, 2013, **393**, 1–20.

8   C. Nilsson, B. Barrios-Lopez, A. Kallinen, P. Laurinmäki, S. J. Butcher, M. Raki, J. Weisell, K. Bergström, S. W. Larsen, J. Østergaard, C. Larsen, A. Urtti, A. J. Airaksinen and A. Yaghmur, A., *Biomaterials*, 2013, **34**, 8491–8503.

9   N. Bye, O. E. Hutt, T. M. Hinton, D. P. Acharya, L. J. Waddington, B. A. Moffat, D. K. Wright, H. X. Wang, X. Mulet and B. W. Muir, *Langmuir*, 2014, **30**, 8898–8906.

10   C. Caltagirone, A.M. Falchi, S. Lampis, V. Lippolis, V. Meli, M. Monduzzi, L. Prodi, J. Schmidt, M. Sgarzi, Y. Talmon, R. Bizzarri and S. Murgia, *Langmuir*, 2014, **30**, 6228–6236.

11   I. Amar-Yuli, D. Libster, A. Aserin and N. Garti, *Curr. Opin. Colloid Interface Sci.*, 2009, **14**, 21–32.

12   J. Barauskas, M. Johnsson, F. Joabsson and F. Tiberg, *Langmuir*, 2005, **21**, 2569–2577.

13   M. Almgren, J. Borné, E. Feitosa, A. Khan and B. Lindman, *Langmuir*, 2007, **23**, 2768–2777.

14   J. Kuntsche, J. C. Horst and H. Bunjes, *Int. J. Pharm.*, 2011, **417**, 120–137.

15   D. Duchêne, G. Ponchel and D. Wouessidjewe, *Adv. Drug Deliv. Rev.*, 1999, **36**, 29–40.

16   J. Zhang and P. X. Ma, *Adv. Drug Deliv. Rev.*, 2013, **65**, 1215–1233.

17   J.R. Lakkakula and R. W. M. A. Krause, *Nanomedicine*, 2014, **9**, 877–894.

18   G. A. Crini, *Chem. Rev.*, 2014, **114**, 10940–10975.

19   P. Zhang, H. Parrot-Lopez, P. Tchoreloff, A. Baszkin, C. Ling., C. de Rango and A. W. Coleman, *J. Phys. Org. Chem.*, 1992, **5**, 518–528.

20   F. Sallas and R. Darcy, *Eur. J. Org. Chem.*, 2008, **2008**, 957–969.

21   E. Bilensoy and A.A. Hincal, *Expert Opin. Drug Deliv.*, 2009, **6**, 1161–1173.

22   U. Kauscher, M. C. A. Stuart, P. Drücker, H.-J. Galla and B. J. Ravoo, *Langmuir*, 2013, **29**, 7377–7383.

23   G. Varan, C. Varan, N. Erdoğar, A. A. Hıncal and E. Bilensoy, *Int. J. Pharm.*, 2017, **531**, 457–469.

24   R. H. de Rossi, O. F. Silva, R. V. Vico and C. J. Gonzalez, *Pure Appl. Chem.*, 2009, **81**, 755–765.

25   F. Quaglia, L. Ostacolo, A. Mazzaglia, V. Villari, D. Zaccaria, M. T. Sciortino, *Biomaterials*, 2009, **30**, 374–382.

26   N. Erdoğar, G. Esendağlı, T. T. Nielsen, M. Şen, L. Öner and E. Bilensoy, *Int. J. Pharm.*, 2016, **509**, 375–390.

27   M. Skiba, D. Duchêne, F. Puisieux and D. Wouessidjewe, *Int. J. Pharm.*, 1996, **129**, 113–121.

28   A. Gèze, J.-L. Putaux, L. Choisnard, P. Jehan and D. Wouessidjewe, *J. Microencapsul.*, 2004, **21**, 607–613.

29   N. R. Pedersen, J. B. Kristensen, G. Bauw, B. J. Ravoo, R. Darcy, K. L. Larsen and L. H. Pedersen, *Tetrahedron: Asymmetry*, 2005, **16**, 615–622.

30   L. Choisnard, A. Gèze, J.-L. Putaux, Y.-S. Wong and D. Wouessidjewe, *Biomacromolecules*, 2006, **7**, 515–520.

31   T. Sun, Q. Guo, C. Zhang, J. Hao, P. Xing, J. Su, S. Li, A. Hao and G. Liu, *Langmuir*, 2012, **28**, 8625–8636.

32   L. Choisnard, A. Gèze, B.G.J. Yaméogo, J.-L. Putaux and D. Wouessidjewe, *Int. J. Pharm.*, 2007, **344**, 26–32.

33   A. Gèze, L. Choisnard, J.-L. Putaux and D. Wouessidjewe, *Mat. Sci. Eng. C*, 2009, **29**, 458–462.

34   J. B.G. Yaméogo, A. Gèze, L. Choisnard, J.-L. Putaux, A. Gansané, S. B. Sirima, R. Semdé and D. Wouessidjewe, *Eur. J. Pharm. Biopharm.*, 2012, **80**, 508–517.

35   E. Lemos-Senna, D. Wouessidjewe, S. Lesieur and D. Duchêne, *Int. J. Pharm.*, 1998, **170**, 119–128.

36   E. Memisoğlu-Bilensoy, A.A. Hincal, A. Bochot, L. Trichard and D. Duchêne, in "Microencapsulation ", S. Benita ed., Taylor and Francis, 2005, Chap. 9, pp. 269–295.

37   A. Mendez-Ardoy, M. Gómez-García, A. Gèze, J.-L. Putaux, D. Wouessidjewe, C. Ortiz Mellet, J. Defaye, J.M. García Fernández and J.M. Benito, *Med. Chem.*, 2012, **8**, 524–532.

38   J. B. G. Yaméogo, A. Gèze, L. Choisnard, J.-L. Putaux, R. Mazet, C. Passirani, M. Keramidas, J.-L. Coll, N. Lautram, J. Béjaud, R. Semdé and D. Wouessidjewe, *Eur. J. Pharm. Biopharm.*, 2014, **88**, 683–694.

39   L. Choisnard, A. Gèze, C. Vanhaverbeke, J. B. G. Yaméogo, J.-L. Putaux, B. Brasme, L. Jullien, S. Boullanger, C. Elfakir and D. Wouessidjewe, *Biomacromolecules*, 2011, **12**, 3031–3038.

40   J.-L. Putaux, C. Lancelon-Pin, F.-X. Legrand, M. Pastrello, L. Choisnard, A. Gèze, C. Rochas and D. Wouessidjewe, *Langmuir*, 2017, **33**, 7917–7928.

41   R. Challa, A. Ahuja, J. Ali and R.K. Khar, *AAPS PharmSciTech.*, 2005, **6**, E329–E357.

42   H. Fessi, J.-P. Devissaguet, F. Puisieux and C. Thies, 1992, US Patent 5,118,528.

43   N. Garti, D. Libster and A. Aserin, *Food Funct.*, 2012, **3**, 700–713.

44   M. Johnsson, Y. Lam, J. Barauskas and F. Tiberg, *Langmuir*, 2005, **21**, 5159–5165.

45   I. Amar-Yuli, E. Wachtel, E. Ben Shoshan, D. Danino, A. Aserin and N. Garti, *Langmuir*, 2007, **23**, 3637–3645.

46   C. Guo, J. Wang, F. Cao, R. J. Lee and G. Zhai, *Drug Discov. Today*, 2010, **15**, 1032–1040.

47   M. Salim, H. Minamikawa, A. Sugimura and R. Hashim, *Med. Chem. Commun.*, 2014, **5**, 1602–1618.

48   G. C. Shearman, O. Ces, R. H. Templer and J. M. Seddon, *J. Phys. Condens. Matter*, 2006, **18**, S1105.

49   D. Hull and D.J. Bacon, in "Introduction to Dislocations", Elsevier, 2011, Chap. 1, pp. 1–20.

50   M. R. Hammond, S. W. Sides, G. H. Fredrickson, E. J. Kramer, J. Ruokolainen and S. F. Hahn, *Macromolecules*, 2003, **36**, 8712–8716.

51   J. Xu, T.P. Russell, B. M. Ocko and A. Checco, *Soft Matter*, 2011, **7**, 3915–3919.

52   M. Komura, H. Komiyama, K. Nagai and T. Iyoda, *Macromolecules*, 2013, **46**, 9013–9020.

53   W. T. M. Irvine, A. D. Hollingsworth, D. G. Grier and P. M. Chaikin, *Proc. Nat. Acad. Sci.*, 2013, **110**, 15544–15548.

54   K. C. Lee and U. Erb, *Arthropod Struct. Dev.*, 2015, **44**, 587–594.

55   K. C. Lee, Q. Yu and U. Erb, *Sci. Rep.*, 2016, **6**, 28342.

56   M. Seul, *J. Phys. I France*, 1994, **4**, 319–334.

57   Y. Liu and B. I. Yakobson, *Nano Lett.*, 2010, **10**, 2178–2183.

58   D. Hull and D. J. Bacon, in "Introduction to Dislocations", Elsevier, 2011, Chap. 9, pp. 171–204.

59   D. H. Warrington, *J. Phys. Colloques*, 1975, **36-C4**, 87–95.

60   J. Thibault, J.-L. Putaux, A. Jacques, A. George, H.-M. Michaud, X. Baillin, *Mat. Sci. Eng. A*, 1993, **164**, 93–100.

61   J. Chen, P. Ruterana and G. Nouet, *Phys. Stat. Sol. A*, 2006, **203**, 247–258.

62   K.C. Lee and U. Erb, *Beilstein J. Nanotech.*, 2013, **4**, 292–299.

63   P. Y. Huang, C. S. Ruiz-Vargas, A. M. van der Zande, W. S. Whitney, M. P. Levendorf, J. W. Kevek, S. Garg, J. S. Alden, C. J. Hustedt, Y. Zhu, J. Park, P. M. McEuen and D. A. Muller, *Nature*, 2011, **469**, 389–393.

64   T.-H. Liu, G. Gajewsk, C.-W. Pao and C.-C. Chang, *Carbon*, 2011, **49**, 2306–2317.

65   P. T. Araujo, M. Terrones and M. S. Dresselhaus, *Mater. Today*, 2012, **15**, 98–109.

66   J. Zhang and J. Zhao, *Carbon*, 2013, **55**, 151–159.

67   Y. Ishida, *J. Mater. Sci.*, 1972, 7, 72–83.

68   L. R. Gómez, N. A. García., R. A. Register and D. A. Vega, *Pap. Phys.*, 2018, **10**, 100001.

69   O. V. Yazyev, *Solid State Comm.*, 2012, **152**, 1431–1436.

70   O. I. Martínez-Muñoz, L. F. Ospina-Giraldo and C. E. Mora-Huertas, in "Nano- and Microencapsulation – Techniques and Applications", InTech Open, N. Abu-Thabit ed., 2021, Chap. 3.

71   E. Lepeltier, C. Bourgaux and P. Couvreur, *Adv. Drug Deliv. Rev.*, 2014, **71**, 86–97.

72   C. J. Martínez Rivas, M. Tarhinia, W. Badri, K. Miladi, H. Greige-Gerges, Q. A. Nazari, S. A. Galindo Rodríguez, R. Álvarez Román, H. Fessi and A. Elaissari, *Int. J. Pharm.*, 2017, **532**, 66–81.

73   X. Xing, H. Shin, M. J. Bowick, Z. Yao, L. Jia, and M.-H. Li, *Proc. Nat. Acad. Sci.*, 2012, **109**, 5202−5206.

74   C. K. Wong, M. Heidelmann, M. Dulle, X. Qiang, S. Förster, M. H. Stenzel, and A. H. Gröschel, *J. Am. Chem. Soc.*, 2020, **142**, 10989−10995.

75   T. I. Gröschel, G. K. Wong, J. S. Haataja, M. A. Dias and A. H. Gröschel, *ACS Nano*, 2020, **14**, 4829−4838.

76   S. D. Hudson, H.-T. Jung, V. Percec, W.-D. Cho, G. Johansson, G. Unger and V. S. K. Balagurusamy, *Science*, 1997, **278**, 449–452.

77   S. D. Hudson, H.-T. Jung, P. Kewsuwan, V. Percec, W.-D. Cho, *Liq. Cryst.*, 1999, **26**, 1493–1499.

78   H.-K. Liu, Y.-L. Ma, L.-J. Ren, C. Kübel and W. Wang, *Langmuir*, 2021, **37**, 10291–10297.

79   D. Demurtas, P. Guichard, I. Martiel, R. Mezzenga, C. Hébert and L. Sagalowicz, *Nat. Commun.*, 2015, **6**, 8915.
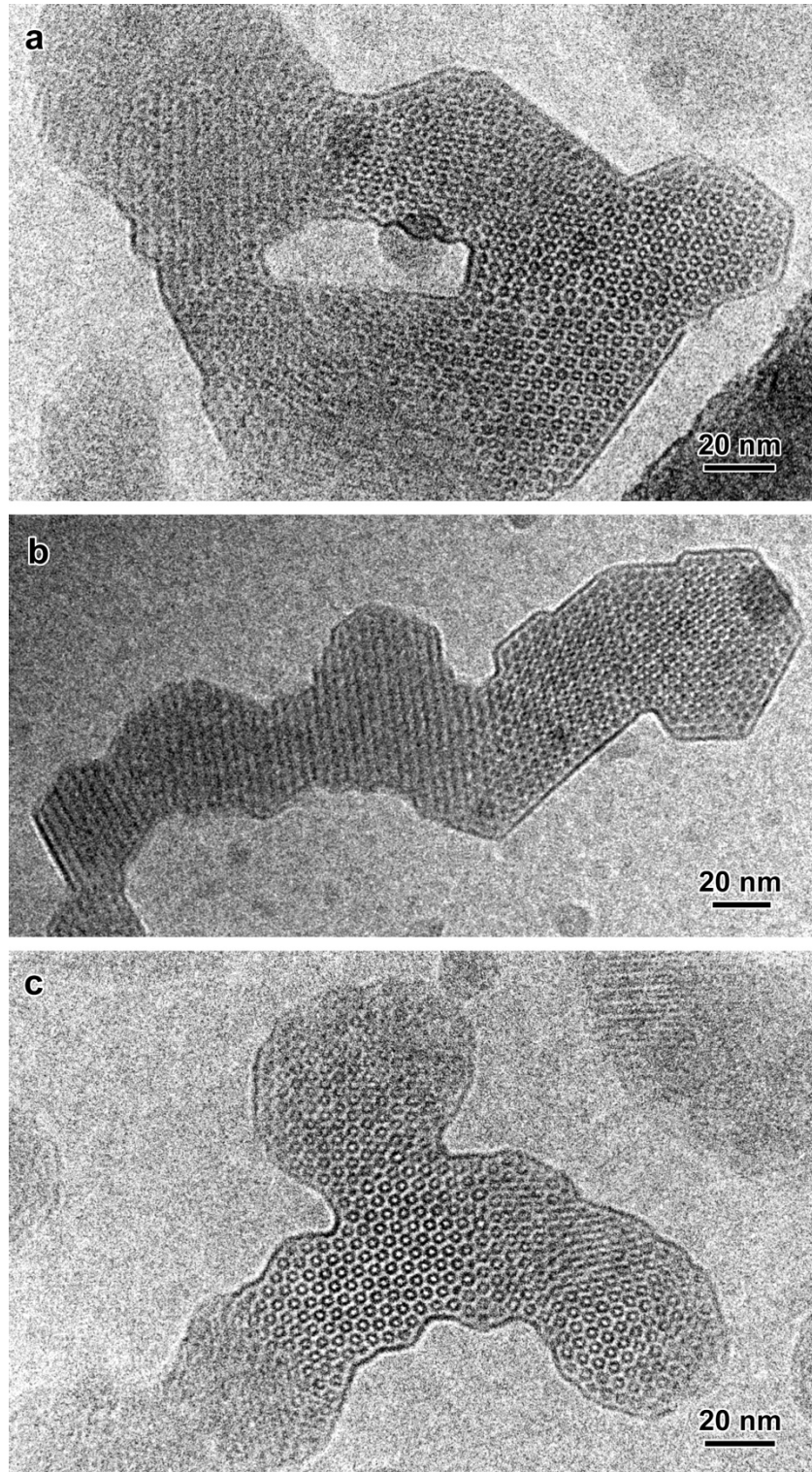
Supplementary Information
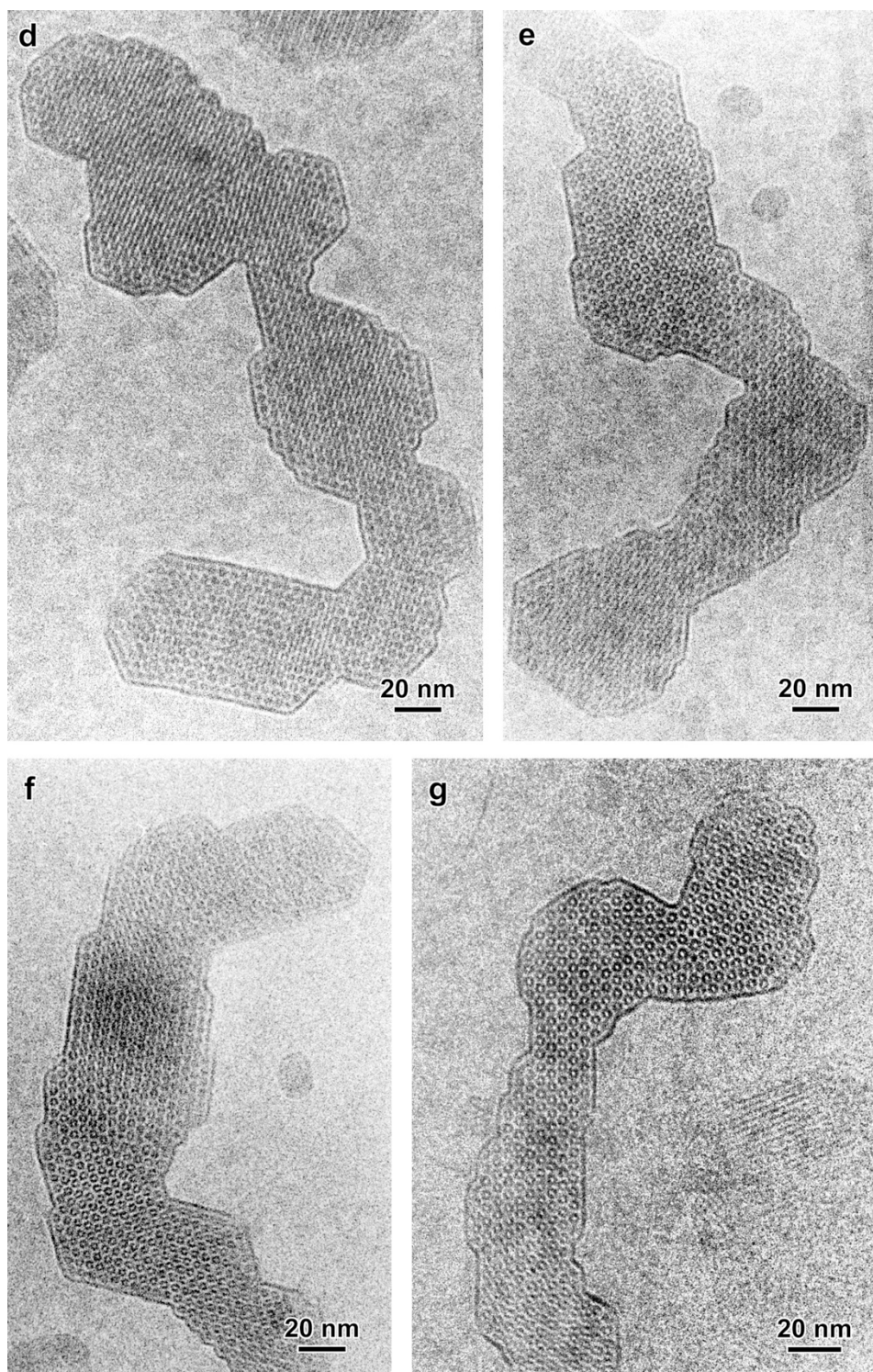

Figure S1. Continued next page.

Figure S1. Cryo-TEM images of various polycrystalline facetted and tortuous βCD-C$_{14}$ particles. Tilt grain boundaries and dislocations in these particles have been described in the main manuscript (**Figures 5-7**).
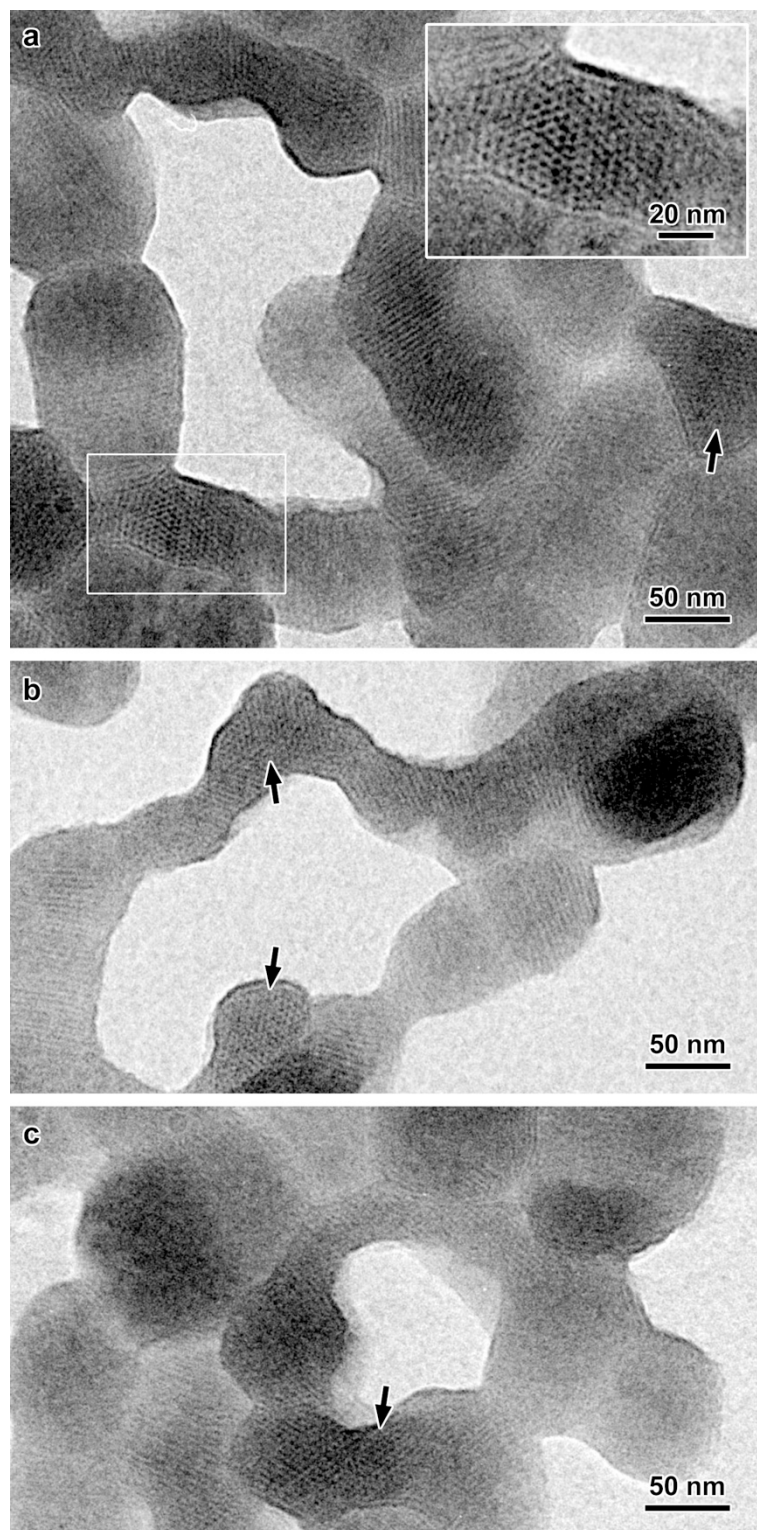
Figure S2. TEM images of polycrystalline βCD-C$_{14}$ particles. After deposition of the suspension and air-drying, the grid was mounted in a Gatan 626 specimen holder and flash-frozen in liquid nitrogen before being transferred in the microscope. The preparation was observed under low dose conditions, at low temperature. The arrows point at regions corresponding to axial projections of the hexagonal columnar organization, exemplified by the inset in image a that corresponds to the framed region.
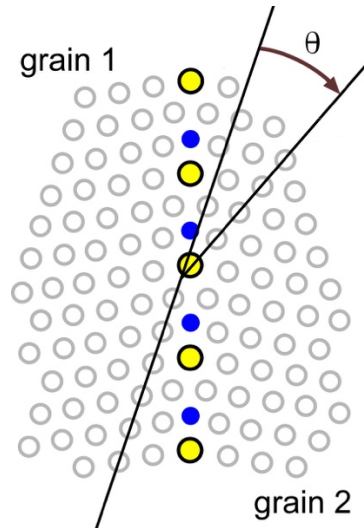
Figure S3. Definition of the tilt angle between two adjacent grains separated by a symmetrical tilt grain boundary. The rotation angle θ between two adjacent grains is defined as the smallest angle between (10) planes from each grain. Example of a Σ = 7 boundary with a tilt angle θ = 21.8°. The yellow and blue disks are columns with 7 and 5 neighboring columns, respectively.
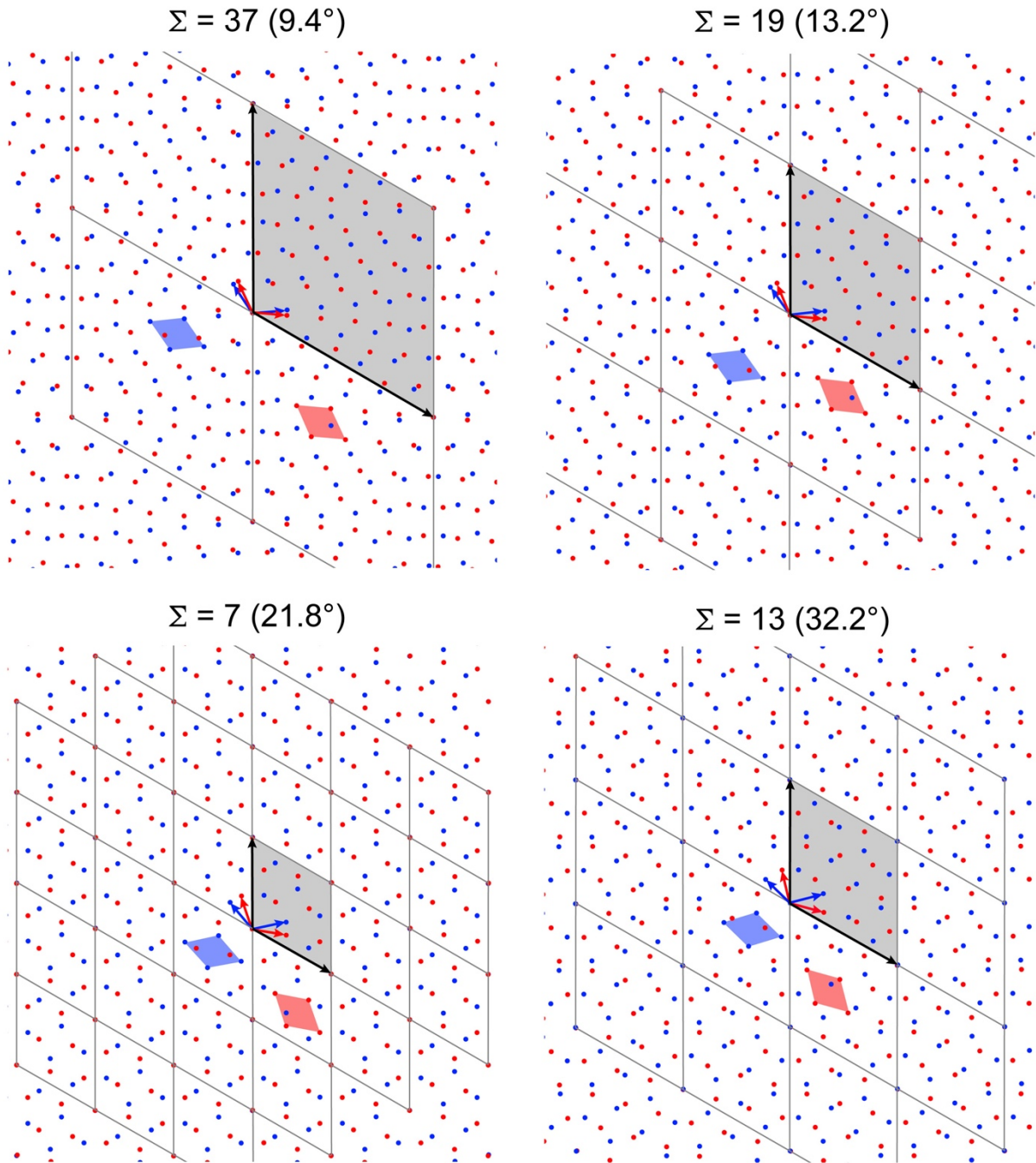
Figure S4. Two-dimensional dichromatic patterns formed by rotating one elementary hexagonal lattice with respect to the other by the angle indicated in parentheses around one site common to both crystals. The elementary lattices are drawn with blue and red dots, respectively, and the unit cells of both lattices are indicated by blue and red rhombi. The coincidence site lattice (CSL), drawn with gray lines, is characterized by the coincidence index Σ defined by the ratio of the surface of the unit cell of the CSL (indicated by a gray rhombus) to that of one elementary lattice. All CSLs have been oriented so that one plane of maximum coincidence is vertical.
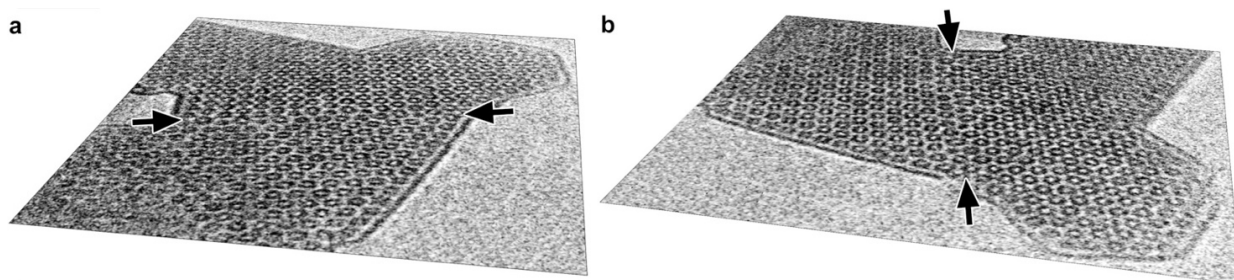
Figure S5. Two views of the cryo-TEM image of the stepped grain boundary analyzed in **Figure 5i-k**. The original image has been rotated to help visualize the tilt angle between the two grains and the local distortion of the lattice planes in the vicinity of the boundary (indicated by arrows). The images have been prepared using the free Blender software (www.blender.org).
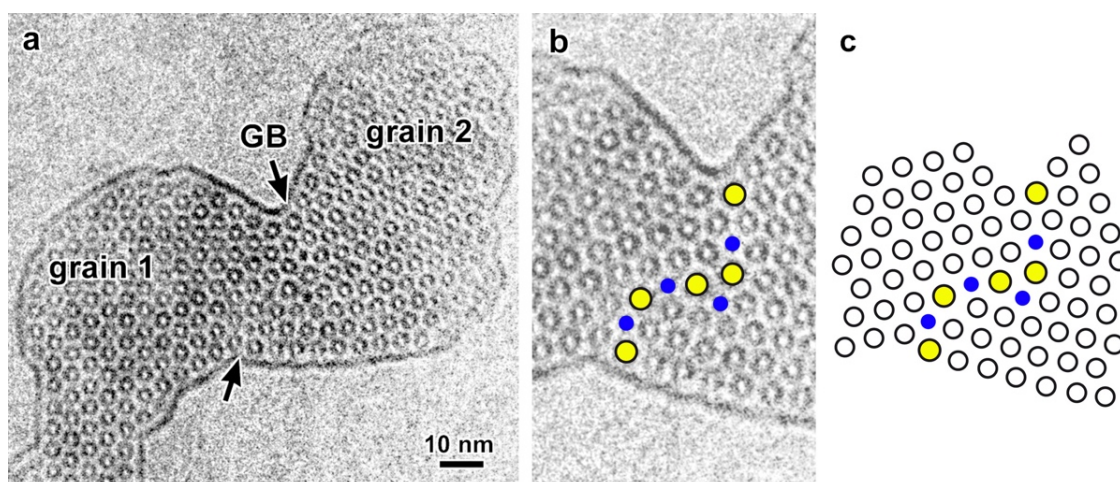

Figure S6. Example of a stepped tilt grain boundary (GB) in a $\beta CD-C_{14}$ multidomain hexosome with a descriptive model of column organization. The black circles are projections of $\beta CD-C_{14}$ columns organized in a hexagonal structure. The yellow and blue disks are columns with 7 and 5 neighboring columns, respectively. The tilt angle measured between the adjacent grains is $25 \pm 1°$. A larger view of the particle is shown in **Fig. S1g**.
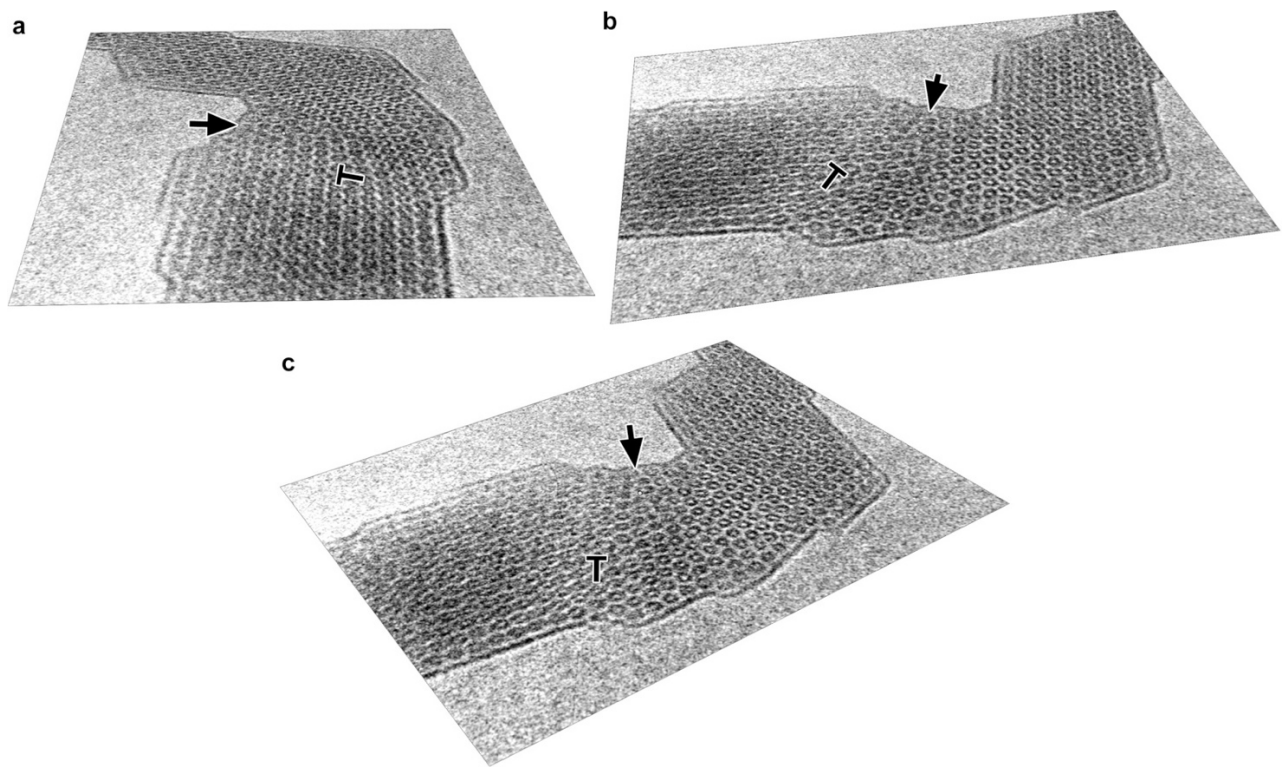
Figure S7. Three views of the cryo-TEM image of the grain boundary and dislocation analyzed in **Fig. 6**. The original image has been rotated to help visualize the tilt angle between the grains and the local distortion of the lattice planes in the vicinity of the boundary (indicated by the arrow) and edge dislocation (T). The images have been prepared using the free Blender software (www.blender.org).